IEEE Access
Multidisciplinary ⋮ Rapid Review ⋮ Open Access Journal

Received 11 September 2026, accepted 2 October 2026, date of publication 8 October 2026, date of current version 20 October 2026.

Digital Object Identifier 10.1109/ACCESS.2026.3741073

RESEARCH ARTICLE

A Monte Carlo Computational Framework Yielding Optimal RF-Dose Bounding for Rodent Bioassays Conducted in Reverberation Chambers

ANTONIO FARAONE[1], (Senior Member, IEEE), GIORGI BIT-BABIK[1], (Senior Member, IEEE), KEVIN SANDERSON[2], PAOLA RUSSO[3], (Senior Member, IEEE), ALFREDO DE LEO[3], (Senior Member, IEEE), VALTER MARIANI PRIMIANI[3], (Senior Member, IEEE), AND VALERIO DE SANTIS[4], (Senior Member, IEEE)

[1]Motorola Solutions, Inc., Fort Lauderdale, FL 33301, USA
[2]University of Toronto, Toronto, ON M5S 1A1, Canada
[3]Università Politecnica delle Marche, 60121 Ancona, Italy
[4]University of L'Aquila, 67100 L'Aquila, Italy

Corresponding author: Antonio Faraone (antonio.faraone@ieee.org)

ABSTRACT Large-scale lifetime rodent bioassays conducted in reverberation chambers (RCs) rely on automated radiofrequency (RF) power control feedback, driven by a sparse set of field probes, to regulate cohort-wide RF energy absorption. As moving rodents load the RC differently from calibration phantoms, the relationship between probe readings and the realized whole-body specific absorption rate (wbSAR) shifts. Compounded by inevitable instrumentation and thermal calibration errors, sparse field sampling may introduce a wider, yet undetected, exposure variance. To quantify and mitigate these effects, a Monte Carlo (MC) dosimetry framework emulating the calibration-to-live experiment chronology, including field-sensing-driven RF-power control, is presented for an RC loaded with 96 male rat models at 900 MHz. Feedback control schemes based on net RF input power and total RF energy density metrics are compared in terms of realized RF dose. Contextualized within historical bioassay parameters, the computational results indicate that compounding sparse field sampling at arbitrary RC locations with said errors induces an unknowable, unrecoverable cage-wise exposure spread, potentially causing dose-group overlaps and over-exposures. To identify optimal probe locations and types, an MC-based selection criterion is demonstrated to substantially mitigate dosimetric spread, bounding cohort-wide exposures within known envelopes and providing a reliable dosimetric design framework for future rodent bioassays.

INDEX TERMS Computational electromagnetics, digital twin, radio-frequency (RF) dosimetry, RF exposure control, reverberation chamber (RC), rodent bioassay, specific absorption rate (SAR).

I. INTRODUCTION

Over the past two decades, reverberation chambers (RCs) have become critical exposure facilities for lifetime, large-scale rodent bioassays aimed at quantifying potential dose-response links between radiofrequency (RF) energy absorption and biological endpoints [1], [2], [3], [4], [5], [6], [7]. For instance, the US National Toxicology Program (NTP) bioassays [8], [9] and the Japanese-Korean (J-K) follow-up [10], [11] featured concurrent exposures of large rodent cohorts to boost statistical power, keeping the RF dose, defined in terms of the whole-body average specific absorption rate (wbSAR) [12], within predefined bounds over two years. Because real-time wbSAR monitoring within caged rodents is physically impossible during bioassays, the exposures are regulated using RF-power feedback-control driven by sparse RC field sampling (e.g., two monitoring field probes in the NTP RCs [8]). Typical calibrations conducted prior to a bioassay yield the baseline link between target RF dose and aggregate probe readings using identical

The associate editor coordinating the review of this manuscript and approving it for publication was Zheng Chen.

© 2026 The Authors. This work is licensed under a Creative Commons Attribution-NonCommercial-NoDerivatives 4.0 License.
For more information, see https://creativecommons.org/licenses/by-nc-nd/4.0/

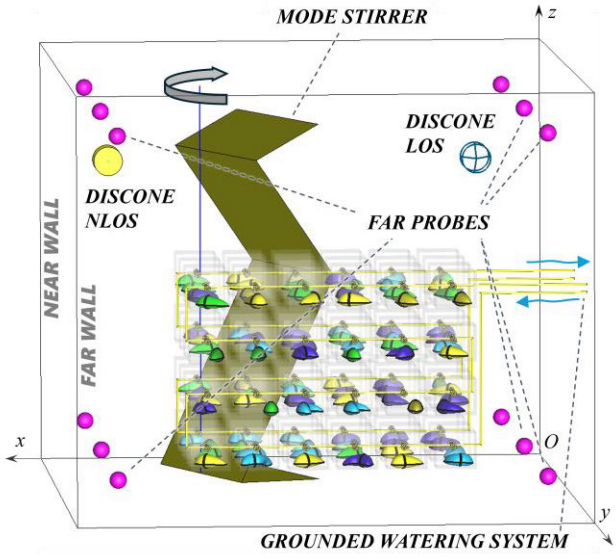

FIGURE 1. TLM digital twin computational model of the rodent-loaded UNIVPM RC. Magenta spheres indicate the locations of the 12 point-wise field probes. Posed adult male rat models are housed in the static 6 × 4 × 4 (in *x*, *y*, *z*) cage arrangement, integrated with the grounded drinking-water delivery system incorporating RF-choked sippers. The NLOS discone antenna is shown as a solid and in wireframe at the LOS location. Probe and watering system details are provided in [17], [18], and [19].

''phantoms'' (e.g., tissue-simulating liquid-filled flasks [4]) loading the RC. However, live rodents exhibit body weight variations across cages as well as changes in posture and position. These factors modify the calibrated relationship between wbSAR and probe readings, resulting in an undetected drift of the global RF dose. Furthermore, the effects on exposure variability arising from sparse field sampling, combined with instrumentation and thermal calibration errors, may not be fully considered when interpreting bioassay outcomes. Based on granular results stemming from realistic full-wave computational modeling, this study provides a quantitative assessment of the RF-dose spread and its dependency on field probe and wbSAR calibration errors, demonstrating significant mitigations achievable through optimal probe configuration choices.

Historically, computational RF dosimetry in RCs relied on idealized, random plane-wave (PW) superposition models [13] capable of exposing single [14], [15] or multiple numerical rodent phantoms [16]. While computationally efficient, random-PW models enforce artificial symmetries that inherently smooth out local field anomalies. Moreover, the only dosimetric link between cohort-averaged wbSAR and probe readings relies on the inherent but untested assumption that, in real RCs, these readings accurately represent the unperturbed incident random-PW field.

Indeed, recent studies employing a highly-detailed, full-wave digital twin model of the Università Politecnica delle Marche (UNIVPM) RC showed that in a realistic, heavily loaded RC, physical boundaries and scattering infrastructure (e.g., metallic drinking-water distribution systems) induce larger exposure asymmetries relative to PW-based estimations [17], [18], [19]. Furthermore, loaded-RC exposures resulted in significantly weaker correlation between individual rodent mass and wbSAR [19], thereby upending the assumption of protective thermal ''mass buffering'' anticipated by random-PW models [16].

Having addressed the *physical* gap inherent in random-PW models, this paper bridges the *operational* gap between static calibration and dynamic *in vivo* exposures in loaded RCs. Section II describes a Monte Carlo (MC) framework that emulates a realistic loaded-RC calibration-to-bioassay chronological scenario based on the full-wave UNIVPM-RC digital twin exposing a 96-adult-rat cohort at 900 MHz. This framework quantifies the impact of distinct RF-dose control metrics (net RF input power, squared field, and total RF energy density) and documented calibration uncertainties on the cohort-wide wbSAR spread. Even under favorable assumptions, the results presented in Section III demonstrate that arbitrary sparse field sampling induces severe exposure variance across cages, which is amplified by the inherent calibration errors. The granular MC outputs yield optimal probe configurations that shrink this variance, thereby providing a reliable *a priori* predictive method to bound dosimetric uncertainty in future *in vivo* RF bioassays. Section IV discusses the applicability of the proposed approach and the implications of the associated findings, while Section V presents the concluding remarks.

II. MONTE CARLO DOSIMETRY FRAMEWORK

The proposed MC framework emulates, in a chronological MC sequence, the static calibration phase and the dynamic experimental phase of a large-scale rodent bioassay at 900 MHz, incorporating realistic instrumentation and calibration errors. However, the RF-dose errors are quantified assuming an ideal RF-power feedback-control scheme with zero latency and no systematic bias, using control variables derived from non-perturbing, sparse RC field sampling. This deliberate idealization provides a favorable scenario that grounds the study findings on traceable error contributors, thus avoiding speculative assumptions regarding other potential errors, e.g., adaptive-control system or environmental drifts.

A. CHAMBER AND COHORT MODELING

The UNIVPM-RC digital twin accurately reproduces its physical dimensions (≈3 m × 4 m × 2.5 m) [20], [21]. Time-domain simulations were performed using the Transmission Line Matrix (TLM) method (CST Studio 2025, Dassault Systèmes). Shown in Fig. 1, the UNIVPM-RC digital twin features a mechanical mode-stirrer, one of three available antennas placed in (non-)line-of-sight (N/LOS) locations relative to the cages [19], and a realistic watering system, modeled after the NTP bioassay RC infrastructure [4], [8], which consists of two metallic serpentines incorporating flanged RF-choked sippers, grounded to a side wall [19].

The chamber is loaded with 96 homogeneous, untailed adult rat models housed in a 6 × 4 × 4 cage lattice, featuring 12% relative standard deviation (R-SD) about the mean cohort mass derived from the historical growth metrics in [8], modeled by a raised-cosine probability density function (PDF), thus preventing unrealistic outliers [16].

Twelve field-sampling probes are defined across the RC, with six of them far from antennas and stirrer (Fig. 1), so as to emulate a large variety of plausible physical sensor networks normally used in bioassays to drive the RF input power feedback-control. These numerical probes, placed at 25 cm (approximate length of commercial miniature probes) from the nearest walls at the RC corners and the midplane between working volume (WV) and stirrer/antennas [19], sample point-wise fields without altering the TLM solution. Both the electric ($\boldsymbol{E}$) and magnetic ($\boldsymbol{H}$) time-domain field waveforms are recorded at each probing location.

B. THE WBSAR CONTROL METRICS

In RF bioassay exposure systems, the input RF power is the manipulated variable setting the animals exposures within predefined ranges. This is usually achieved through feedback mechanisms governed by suitable control variables. Typically, RF generator settings are adjusted (e.g., every 20 s in the NTP bioassays) in response to sampled RF energy metrics derived from field probes placed within the system. Linking internal RF-dose metrics such as the wbSAR with external fields within the exposure system frequently relies on an experimental *dosimetric factor* (DF) [19].

Following each TLM simulation, corresponding to a given stirrer angle, the computed wbSARs and sampled-field 900 MHz phasors are normalized to the net RF input power metric $\left(\Psi_P = P_{inc} - P_{ref}\right)$ before any postprocessing, thus removing the antenna reflection coefficient variability with RC loading and stirrer angle from the subsequent dosimetric analysis. This choice decouples antenna-specific impedance sensitivities, representing a potential confounder, from the analysis, while leaving the intended differentiating antenna characteristics such as size and directivity pattern intact. This scenario emulates zero-latency compensation for impedance variability, restoring the nominal net RF input power. Such a favorable scenario underpins the wbSAR feedback-control emulation architecture described in Section II-C, which relies on the RF energy metrics defined in Section II-B1.

1) AGGREGATE ELECTROMAGNETIC ENERGY DENSITY METRICS

In the following, the subscript (E, H, U) identifies the energy metric domain (electric, magnetic, or total energy density), while spatial aggregation is denoted by an overline $\bar{(\cdot)}$ for arithmetic means and a caron $\check{(\cdot)}$ for medians.

Let $\mathcal{P}_E$ denote a combination of N_E $\boldsymbol{E}$-field probes across $N_P = 12$ available locations. The aggregate electric energy density metric (Ψ_E) is evaluated using either the arithmetic mean or, for sufficiently large N_E, the median descriptor:

$$\overline{\Psi}_E = \frac{1}{N_E} \sum\nolimits_{j\in\mathcal{P}_E} \frac{1}{2}\epsilon_0 \left|\boldsymbol{E}_j\right|^2_{rms}, \tag{1a}$$

$$\check{\Psi}_E = \underset{j\in\mathcal{P}_E}{\text{median}} \left\{ \frac{1}{2}\epsilon_0 \left|\boldsymbol{E}_j\right|^2_{rms} \right\}, \tag{1b}$$

where ϵ_0 is the vacuum permittivity, while $\left|\boldsymbol{E}_j\right|_{rms}$ denotes the j-th probe *rms* $\boldsymbol{E}$-field magnitude reading. The aggregate magnetic energy metric (Ψ_H) is similarly defined over a subset $\mathcal{P}_H$ of N_H $\boldsymbol{H}$-field probing locations, with the vacuum permeability μ_0 in lieu of ϵ_0. Both field metrics are computed for each RC field realization and ensemble averaged across stirrer angles (denoting with $\langle\cdot\rangle$ the stirrer-state averaging). The practical limitation to place either an $\boldsymbol{E}$- or an $\boldsymbol{H}$-field probe at a given probing location yields $\mathcal{P}_E \cap \mathcal{P}_H = \emptyset$. Hence the joint set $\mathcal{P}_U = \mathcal{P}_E \cup \mathcal{P}_H$ identifies $N_U = N_E + N_H$ locations used to define the total RF energy density aggregate metric in balanced terms as follows:

$$\Psi_U = \frac{N_E\Psi_E + N_H\Psi_H}{N_U}, \tag{2}$$

where the metrics Ψ_E, Ψ_H both utilize the same statistical descriptor (mean or median).

Upon choosing an aggregate metric $\Psi_X, X \in \{E, H, U\}$, the MC framework emulates the complete calibration-to-bioassay operational workflow subject to compound probe reading and dosimetric calibration errors. As detailed in Section II-E, running these scenarios for every probe configuration yields a granular picture of each caged rodent statistical wbSAR outcomes. As shown in Section III-C, an exhaustive search yields the optimal probe configurations that substantially narrow the cohort-wide RF-dose spread, informing the RC probe deployment *a priori*.

The variability range of these aggregate metrics is large. For example, placing $N_U = 4$ $\boldsymbol{E}$-field probes across the 12 available locations in Fig. 1 (495 possible configurations; no type permutations in this case) yields the range shown in Fig. 2 for the aggregate error-free means. Similar multi-modal, broad distributions are consistently observed across varying probe counts (hence location combinations) and types ($\boldsymbol{E}$, $\boldsymbol{H}$), indicating an inherent stochastic spread of these metrics.

C. EMULATION OF CALIBRATIONS AND EXPERIMENTS

The MC framework combines the RC spatial field variations (function of the RC load and stirrer angle) with the rodents' randomized mass, posture, cage location and orientation, by shuffling independently the states of the 96 caged models over 36 stirrer angles (10° step) [19]. As identical calibration phantoms are typically preferred, their mass was scrambled only in the live-experiment emulations. Select cases were run with 72 stirrer angles (5° step) producing statistically equivalent ensemble-averaged and instantaneous wbSAR distributions as with 10° steps.

In the following, superscripts denote the operational phases: *cal* for calibrations and *live* for live experiments

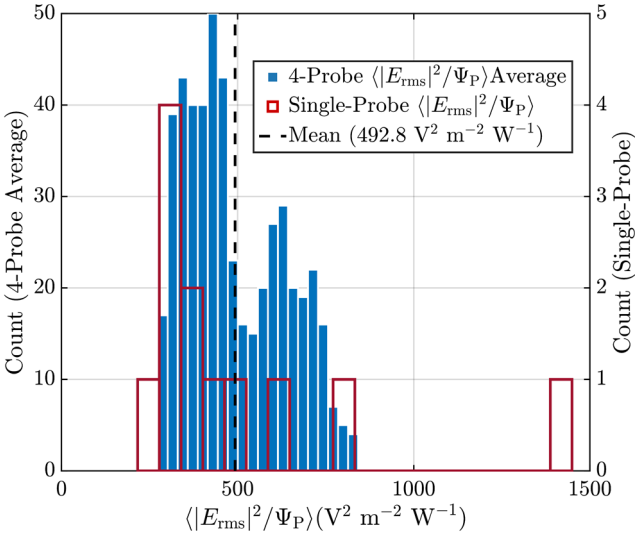

FIGURE 2. Ensemble-averaged squared *rms* E-field normalized readings at the $N_P = 12$ probing locations shown in Fig. 1 (red histogram), and associated mean values across all possible combinations of $N_U = 4$ probe locations (blue). The respective means (dashed line) coincide. Live-experiment emulation featuring 650 g mean cohort weight, the discone NLOS setup, including the watering system infrastructure.

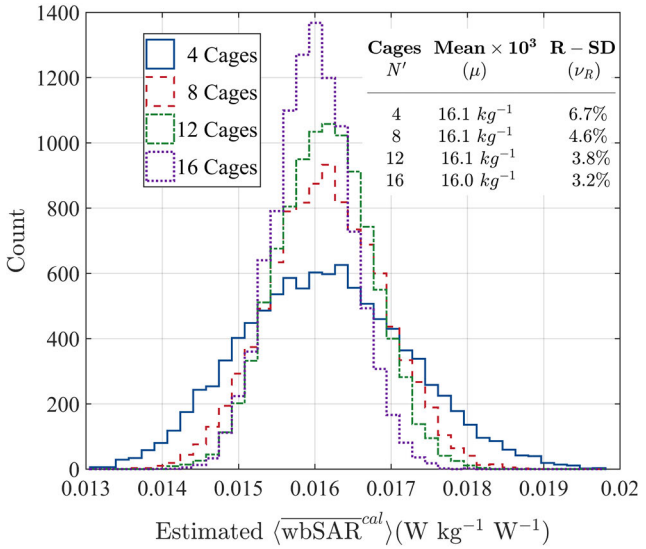

FIGURE 3. Histograms of cohort-wise mean RF-dose estimates from subsets of 4, 8, 12, or 16 out of 96 caged phantoms sampled randomly across topological cage categories (error-free calibrations; 650 g mean cohort weight; discone NLOS setup; watering infrastructure). Datasets generated via 10,000 MC realizations and normalized to the net RF input power. While the means (μ) remain insensitive in this example, the respective R-SDs (ν_R) decrease steadily with the sample size.

(bioassay). The term "RF dose" will refer to the ensemble-averaged wbSAR, which governs the RF-induced heat load.

1) EMULATION OF THE DOSIMETRIC CALIBRATION SETUP

Prior to the live bioassay emulation, a baseline relationship is established between a predefined RF-dose metric and the external field metric (or the net RF input power at the RC antenna feed), yielding a corresponding *calibrated*-DF. The mean of the cage-wise, ensemble-averaged wbSARs is the typical RF-dose metric chosen in large-scale bioassays (e.g., [8], [9], [10], [11]). Its determination usually involves estimating the RF energy absorption in several calibration phantoms by means of whole-body temperature-rise evaluations [4], [22], [23]. Consequently, the overall *calibrated*-DF uncertainty stems in part from the sparse phantom sampling if only a practical subset of phantoms (e.g., from 4 to 16) is evaluated, rather than the entire set. For example, in the NTP mouse bioassays [9], temperature probes were installed in four phantoms, which were moved to ten random positions [14].

The proposed MC framework enables isolating this subsampling impact on the overall calibration uncertainty, as in the example in Fig. 3 featuring 4 to 16 sampled phantoms chosen at random across each topological category (*corner*, *edge*, *face*, *inner* cages), thereby preserving the associated RF-dose imbalances [19]. Neglecting wbSAR evaluation errors in order to isolate the subsampling uncertainty contribution, the corresponding histograms show that sampling 16 of 96 phantoms yields a narrow error (3.2% R-SD), which steadily doubles going down to just 4 phantoms (6.7% R-SD). Although these calibration variances appear small enough to justify adopting cage subsampling, their unrecoverable impact on RF-dose spread (showcased in III-D) may actually suggest boosting the number of samples.

In a typical calibration, holding identical phantoms (e.g., flasks) fixed inside cages over multiple stirrer revolutions, as temperatures evolve, can bias their RF-dose estimates if they occupy a "cold" or "hot" RF spot. To avoid this, the emulated positions and orientations of all 96 phantoms are shuffled at each stirrer step (field realization). Hence, randomly "stirring the phantoms" alongside the RC fields yields an unbiased cage-wise *calibrated*-DF:

$$\mathrm{DF}^{cal}_{X,n} \overset{\text{def}}{=} \frac{\langle \mathrm{wbSAR}^{cal}_n \rangle}{\langle \Psi^{cal}_X \rangle}, n = 1, \ldots, N, \tag{3}$$

where Ψ^{cal}_X is the chosen aggregate field metric, while wbSAR^{cal}_n represents the n-th rat model RF dose computed for a given stirrer angle, and N is the number of cages. Since thermal processes evolve much slower than the RC fading dynamics, averaging wbSAR^{cal}_n across RC field realizations yields the appropriate cage-wise heat-load proxy [19].

If $\mathcal{S}_{cal}$ is a subset comprising $N' = |\mathcal{S}_{cal}| \leq N$ monitored cages during calibrations, the cohort-wise mean RF dose is:

$$\left\langle \overline{\mathrm{wbSAR}}^{cal} \right\rangle = \frac{1}{N'} \sum\nolimits_{n \in \mathcal{S}_{cal}} \left\langle \mathrm{wbSAR}^{cal}_n \right\rangle, \tag{4}$$

which yields the cohort-wise *calibrated*-DF

$$\overline{\mathrm{DF}}^{cal}_X \overset{\text{def}}{=} \frac{\left\langle \overline{\mathrm{wbSAR}}^{cal} \right\rangle}{\langle \Psi^{cal}_X \rangle} = \frac{1}{N'} \sum\nolimits_{n \in \mathcal{S}_{cal}} \mathrm{DF}^{cal}_{X,n}. \tag{5a}$$

For large N', the median provides a suitable alternative:

$$\widetilde{\mathrm{DF}}^{cal}_X \overset{\text{def}}{=} \frac{\mathrm{median}_{n \in \mathcal{S}_{cal}} \left\{ \langle \mathrm{wbSAR}^{cal}_n \rangle \right\}}{\langle \Psi^{cal}_X \rangle} = \underset{n \in \mathcal{S}_{cal}}{\mathrm{median}} \left\{ \mathrm{DF}^{cal}_{X,n} \right\}. \tag{5b}$$

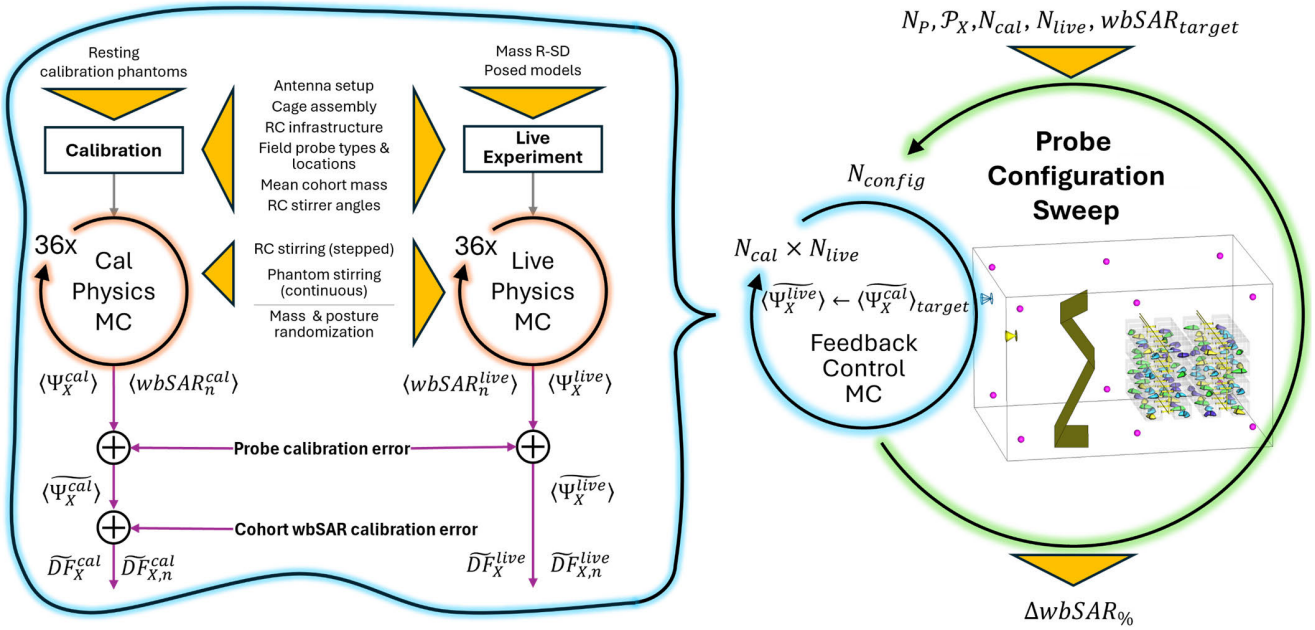

FIGURE 4. Flowchart of the hierarchical MC architecture. The *physics* MC engine (left) feeds the control parameters to the *control* MC engine (right). The 36-step stirrer revolutions emulate the *calibration* and *live* experiment physics, yielding error-free, ensemble-averaged outputs. Field probe and cohort-wise mean wbSAR calibration errors are superimposed to generate the error-corrupted dosimetric factors yielding the RF-dose error distributions for a given probe configuration. The *control* MC engine retrieves the error-corrupted control parameters and its feedback controller forces the real-time experimental field metric to coincide with the target value by regulating the net RF input power at the RC antenna feed-point. The outermost sweep cycles through every available probe configuration and yields the corresponding cage-wise RF-dose error distributions.

Rather than adopting some arbitrary flask-like phantom, the emulated calibrations rely on the "resting" phantoms used in live-experiment emulations [19], thus approaching similar RC loading while avoiding a potential confounder.

2) EMULATION OF THE LIVE BIOASSAY SETUP

Compared with calibrations, where position and orientation of identical rat models in the respective cages are reshuffled at each sequential stirrer angle, live-experiment emulations feature four equiprobable posed models (resting, elongated, asleep clockwise or counter-clockwise) resembling those identified in [14] from video footage and historical data, as well as concurrent mass randomization according to a raised-cosine distribution with 12% R-SD centered at 650 g [16], [19]. The *live*-DF can then be expressed, similarly to (5), as

$$\overline{\mathrm{DF}}_X^{live} = \frac{1}{N}\sum_{n=1}^{N} \mathrm{DF}_{X,n}^{live} = \frac{1}{N}\sum_{n=1}^{N} \frac{\langle \mathrm{wbSAR}_n^{live} \rangle}{\langle \Psi_X^{live} \rangle} = \frac{\overline{\mathrm{wbSAR}}^{live}}{\langle \Psi_X^{live} \rangle}, \tag{6a}$$

or, in terms of cohort-wise median, as

$$\widetilde{\mathrm{DF}}_X^{live} = \frac{\mathrm{median}_{1\le n\le N}\left\{\langle \mathrm{wbSAR}_n^{live} \rangle\right\}}{\langle \Psi_X^{live} \rangle} = \underset{1\le n\le N}{\mathrm{median}}\left\{\mathrm{DF}_{X,n}^{live}\right\}, \tag{6b}$$

where Ψ_X^{live} stems from the *live* experiment using the same aggregate metric adopted in the calibration. Observe that the cohort-wise RF doses in (6) take into account all N rodents, thus yielding the realized, error-free, mean (or median) cohort-wise exposure. Table 1 compares the salient aspects and features of the calibration and live-experiment phases.

TABLE 1. Monte Carlo emulation parameters for the calibration and live experiment phases.

Parameter	Calibration Phase Emulation (*cal*)	Live Experiment Phase Emulation (*live*)
Cohort	96 identical *resting* phantoms	96 phantoms with different posture and mass
Mass Distribution	Nominal target mass in all 96 cages	Raised-cosine mass distribution (12% R-SD)
Phantom Shape/ Posture	Fixed shape (matching the "resting" posture) across the entire cohort	Uniformly randomized posture (resting, elongated, sleeping CW or CCW [16])
Position & Orientation	Uniformly randomized at each stirrer angle	Uniformly randomized at each stirrer angle
MC Goal	Spatially unbiased baseline	Realistic mass variance & posturing, and roaming
Key Outputs	$\overline{\mathrm{DF}}_X^{cal}$ and $\widetilde{\mathrm{DF}}_X^{cal}$	$\mathrm{DF}_{X,n}^{live}$, $\overline{\mathrm{DF}}_X^{live}$, $\widetilde{\mathrm{DF}}_X^{live}$

3) EMULATION OF THE RF INPUT POWER CONTROL

While real-world controllers feature inertia, latency, and hysteresis, the calibration and live-experiment phases in the emulated closed-loop scenario are reciprocally anchored via an ideal RF-power controller model, free of bias and drift, featuring zero-latency response to real-time aggregate probe readings affected by the inevitable calibration errors (e.g., [4, Table 5]). In reality, although closed-loop control hardware introduces processing latencies in the order of seconds, the thermal time constants governing rodent

physiological heat dissipation are measured in minutes. Conversely, sensor drift might go unnoticed unless process and data integrity controls are implemented, particularly over wireless telemetry relays [24], [25]. Adopting an idealized zero-latency, drift-free baseline isolates calibration and field-sampling error contributors to exposure variance, grounding the ensuing findings on error contributors traceable to prior bioassays.

Setting the target RF dose (wbSAR_{target}) in terms of cohort-wise mean (or median) as in (5), the corresponding aggregate metric target is computed from the *calibrated*-DF:

$$\left\langle \Psi_X^{cal} \right\rangle_{target} = \frac{\mathrm{wbSAR}_{target}}{\mathrm{DF}_X^{cal}}. \tag{7}$$

The term DF_X^{cal} is denoted generically here as its statistical descriptor (mean or median) has to align with the dosimetric choice made for wbSAR *target*, whereas $\left\langle \Psi_X^{cal} \right\rangle_{target}$ has to match the $\left\langle \Psi_X^{cal} \right\rangle$ descriptor adopted in (3) and used in the DF definitions (5), which constitutes a control choice.

During live experiments, the idealized control loop tunes the RF power impinging at the antenna to force the aggregate energy metric to match the target defined in (7)

$$\left\langle \Psi_X^{live} \right\rangle \leftarrow \left\langle \Psi_X^{cal} \right\rangle_{target}. \tag{8}$$

TABLE 2. Summary of electromagnetic metrics, dosimetric factors, and operational constraints.

Category	Symbol	Definition	Operational Role & Constraints
Field Sensing	Ψ_X	Aggregate RF energy density ($X \in \{E, H, U\}$)	Computed per stirrer angle across N_X probes; aggregated via the mean or median
Target Setting	wbSAR_{target}	Predefined desired cohort-wide dose rate	Its statistical nature (mean vs. median) is inherited from the definition of DF_X^{cal}
Calibration Baseline	$\overline{\mathrm{DF}}_X^{cal}$ $\widetilde{\mathrm{DF}}_X^{cal}$	Ratio of the baseline dose over S_{cal} to the aggregate RF energy metric	Sets the aggregation operator (mean or median) employed in the power-control feedback-loop
Controller Input	$\langle \Psi_X^{cal} \rangle_{target}$	Target energy metric required to achieve wbSAR_{target}	The net RF input power is clamped to set the live fields to match this target
Live Reality	$\mathrm{DF}_{X,n}^{live}$ $\overline{\mathrm{DF}}_X^{live}$ $\widetilde{\mathrm{DF}}_X^{live}$	Ratio of the actual RF dose to the live aggregate RF energy	Captures the inherent spatial and biological variance of the live cohort
Key Outcomes	wbSAR_{live}	Ideal error-free cohort-wise RF dose realized by the system	Realized equivalent of the predefined target; captures the controller bias, without error
	$\widetilde{\mathrm{wbSAR}}_{X,n}^{live}$	Actual RF dose to the nth individually caged rodent	Compounds the inherent cage-wise spread and the controller bias, and includes errors

From the *live*-DF defined in (6), dropping the diacritics, enforcing (8) yields the cohort-wise wbSAR:

$$\mathrm{wbSAR}_{live} = \mathrm{DF}_X^{live} \cdot \left\langle \Psi_X^{live} \right\rangle \leftarrow \frac{\mathrm{DF}_X^{live}}{\mathrm{DF}_X^{cal}} \mathrm{wbSAR}_{target}. \tag{9}$$

Even though "phantom stirring" mitigates spatial bias in calibrations, a *global controller bias* (DF_X^{live}/DF_X^{cal}) indeed arises, due to the RC loading differences between calibration and live experiment, shifting the final RF dose:

$$\Delta\mathrm{wbSAR}_{\%} = 100 \times \left(\frac{DF_X^{live}}{DF_X^{cal}} - 1 \right). \tag{10}$$

The energy density aggregation operators $\left(\left\langle \Psi_X^{cal} \right\rangle, \left\langle \Psi_X^{live} \right\rangle\right)$ in (8) must conform to the same statistical descriptor. The same holds for DF_X^{cal} and DF_X^{live} in (9) and consequently for wbSAR_{target} and wbSAR_{live}.

D. RF-DOSE SPREAD DUE TO CALIBRATION ERRORS

The cohort RF-dose control described in II-C hinges on: probe types and locations; the statistical descriptor chosen for Ψ_X; physical field probe calibration errors; and the cage-wise wbSAR thermal calibration error (e.g., [14, Table 5]). These errors propagate into $\widetilde{DF}_{X,n}^{cal}$ (the tilde denoting error-corruption), thus into $\widetilde{DF}_X^{cal}$ and then into $wbSAR_{live}$ via (9). Analogously, live-experiment probe-reading errors trickle into $wbSAR_{live}$ in (9) via $\widetilde{DF}_X^{live}$, computed in (6) using the error-corrupted metric $\left\langle \widetilde{\Psi}_X^{live} \right\rangle$. These calibration errors are superimposed onto the respective TLM simulation results as shown in the hierarchical MC architecture in Fig. 4.

Within this context, only systematic errors that persistently alter the realized RF dose are considered, such as field probe reading deviations introduced during calibration, and the offset between true and estimated mean cohort-wise wbSAR from the experimental determination of the *calibrated*-DF. Conversely, electronic noise and transient drifts (e.g., caused by short-lived thermal gradients in the RC) are presumed to average out. The overall impact of these systematic errors is quantified in Section III.

The proposed MC framework leads to cage-wise live RF-dose estimates for each probe configuration, thereby yielding a range of possible realized RF doses for each caged rodent. Enforcing (8) marks the crucial transition from an open-loop unconstrained quantity to a closed-loop regulated one: while the RF dose $\left\langle \mathrm{wbSAR}_n^{live} \right\rangle$ in (6) does not depend on the metric Ψ_X associated with a given probe configuration, closing the feedback loop via (8) locks the n-th cage realized RF dose to this metric. Upon incorporating the error-corrupted DFs, the realized cage-wise dose is tied to the cohort-wise target as follows:

$$\left\langle \widetilde{\mathrm{wbSAR}}_{X,n}^{live} \right\rangle = \left(\frac{\widetilde{\mathrm{DF}}_{X,n}^{live}}{\widetilde{\mathrm{DF}}_X^{live}} \right) \left(\frac{\widetilde{\mathrm{DF}}_X^{live}}{\widetilde{\mathrm{DF}}_X^{cal}} \right) \mathrm{wbSAR}_{target}, \quad n = 1, \ldots, N. \tag{11}$$

Here, the subscript X formally distinguishes the *realized* wbSAR from the unconstrained RF dose in (6).

TABLE 3. Summary of stochastic variables and injected errors within the hierarchical Monte Carlo architecture.

Stochastic Variable / Error Component	Emulation Phase		Distribution Model	Variance / Bounds / Categories
	Cal.	Live Exp.		
Rodent Mass [8, Tables 17 and 44]	No	Yes	Raised-Cosine	650 g mean with 12.0% R-SD
Rodent Posture [16]	No	Yes	Uniform (Categorical)	Resting, Elongated, Sleeping CW & CCW
Rodent Position & Orientation [16]	Yes	Yes	Uniform (Continuous)	Bounded by respective cage walls
Probe Calibration Error [4, Table V]	Yes	Yes	Raised-Cosine	9.1% R-SD
Cage-wise wbSAR Temperature Probe Error [a]	Yes	No	Raised-Cosine	11.8% R-SD (applied to cage-wise RF doses)
Other Cohort-wise wbSAR Calibration Errors [b]	Yes	No	Raised-Cosine	10.7% R-SD (applied to the cohort-wise avg.)

([a]): Calculated from the *temperature probe* standard error (1.2%) reported in [14, Table V] as $1.2\% \times \sqrt{96} \approx 11.8\%$.

([b]): Calculated from the *field control* (4.7%) and *RC temperature fluctuations* (9.6%) error components in [14, Table V] via quadrature summation.

Writing (11) in terms of cascading ratios cleanly separates its physical and operational drivers. The first ratio captures the inherent physics, governed by the RC geometry and the caged rodent location, morphology, and dynamics, yielding the cohort-wide wbSAR spread. The second ratio is the realized global controller bias, which modulates the physics-driven variance. For example, the inherent spread among cages is amplified if the controller bias exceeds unity. Table 2 provides a summary of the MC framework core metrics, dosimetric factors, and operational drivers.

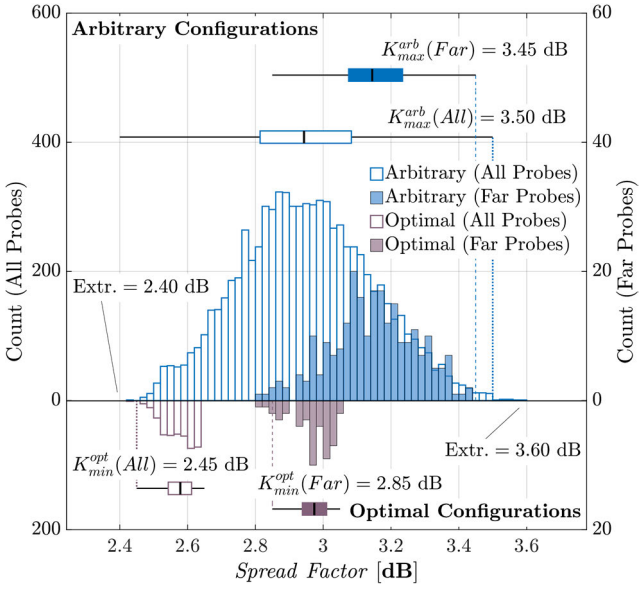

FIGURE 5. Realized spread factors across sparse probe configurations ($N_U = 4$) in a discone NLOS setup (watering system present). The top histograms refer to 7920 arbitrary configurations (hollow blue, left axis) and 240 far-probe ones (solid blue, right axis) featuring upper Tukey's boxplot whiskers K^{arb}_{max}. The inverted histograms refer to the respective *KFF*-optimal configurations ($\gtrsim$5% and 20% share of respective totals) featuring lower whiskers K^{opt}_{min}. Extreme distribution bounds are marked. All values rounded to 0.05 dB.

The granularity of the emulated results yields cage-specific histograms, hence quantifiable expectations of the cage-wise RF-dose ranges. As shown in Section III, distinct RC arrangements can be ranked in terms of RF-dose spread under diverse scenarios. For instance, the idealized scenario outlined thus far, where latency, drifts, and spatial biases were neutralized to isolate calibration errors and sparse RC field sampling effects, can be augmented to include other known error sources and yield a more prudent assessment.

E. STOCHASTIC VARIABLES AND MC IMPLEMENTATION

The proposed MC architecture is hierarchically structured to inject distinct dosimetric uncertainty sources, listed in Table 3. To achieve this, the architecture in Fig. 4 is divided into two nested blocks: a *physics* MC engine that generates the error-corrupted calibration and control parameters, which are subsequently fed into the *control* MC engine.

The *physics* MC engine incorporates the parallel execution of the calibration and live experiment phases, featuring the RC arrangements detailed in Table 1, to extract the error-free, ensemble-averaged metrics across 36 stepped stirrer angles. Random probe and cohort-wbSAR calibration errors are then superimposed, yielding error-laden parameters. Reacting to these inputs, the *control* MC engine defines the controller target via (7) based on the specific probe configuration called within the outermost sweep, and then forces the *live* net RF input power alignment via (8). Hence, the resulting cage-wise wbSAR distributions reflect the regulating impact of each swept probe configuration with fine granularity.

The total number of probe configurations swept in the outermost loop is given by the size of the Cartesian product of the set of all probing location combinations ($\mathcal{C}_{loc}$) and the associated set of probe-type permutations ($\mathcal{P}_{type}$):

$$N_{config} = \left|\mathcal{C}_{loc} \times \mathcal{P}_{type}\right| = \binom{N_P}{N_X} \cdot b^{N_X}, \qquad b = \begin{cases} 1, & X \in \{E, H\} \\ 2, & X = U. \end{cases} \tag{12}$$

To emulate the operational lifecycles of realistic bioassays, where a single calibration typically governs weeks or months of daily live experiments across many RCs, the *control* MC engine encompasses a deeper nested loop. For a given probe configuration, N_{cal} independent calibrations (i.e., involving uncorrelated calibration errors) govern N_{live} independent live experiment emulations each, forced into compliance with the latest calibration via the controller loop. This architecture reflects practical realities, while avoiding that a singular anomalous calibration skew the exposure error distributions.

The proposed MC architecture may be executed for any particular RC arrangement, encompassing a specific antenna

type and location, infrastructure (stirrers, watering system), and biological load (e.g., cage assembly, rodent weights and dynamics), cycling through all the probe configurations.

III. RESULTS

This section quantifies in fine detail the RF-dose spread for the highly realistic, loaded RC digital twin in Fig. 1 with 96 caged rat models (650 g mean weight, representative of adult male rats [8, Tables 17, 44]), housed in a 6 × 4 × 4 cage assembly integrated with a grounded watering system featuring flanged RF-choked sippers [19]. The ensemble-averaged wbSAR for each caged rat model, indicative of the RF-induced heat load, represents the key observable.

The MC random variables and the nested-loop parameters are described first, followed by the definition of a suitable figure of merit for the RF-dose spread. Next, a preliminary analysis evaluates the impact of probe calibration errors on the cohort-wide wbSAR spread, using the U-dipole NLOS setup due to its narrowest cage-wise exposure imbalances (Table 4). In contrast, the core results subsequently center primarily on the discone NLOS setup, which serves as the most representative case due to its median imbalances.

The arithmetic mean of the total RF energy (i.e., $X = U$) is the adopted control metric in all cases. Appendix A outlines the associated feedback-control regulation details.

A. MC ANALYSIS OF THE RF-DOSE SPREAD

Mirroring other provisions aimed at avoiding confounders (zero-latency, bias/drift-free controller; ''resting'' calibration phantoms; ''phantom stirring''; bounded error distributions), the subsampling error of Fig. 3 is neutralized by setting $N' = N$ in (4)-(5). Notably, all the phantoms were probed during thermal calibration in the NTP rat bioassay [14]. However, to prevent overly optimistic RF-dose spread estimates from masking potentially unmitigated thermal loads or dose-group overlaps, the RF-dose range is quantified using select lower and upper statistical percentiles of the cage-wise *live* wbSAR distributions. In particular, over the $N_{cal} \times N_{live}$ MC realizations run for each swept probe configuration, the *control* MC engine tracks the minimum of the 10th percentiles and the maximum of the 90th percentiles across cage-wise RF doses. The resulting PDFs yield a granular picture of the exposure spread observed across all available probe configurations. With $N = 96$, these outer percentiles leave approximately

TABLE 4. Maximum cage-wise ensemble-averaged wbSAR imbalance across antenna configurations (650 g mean cohort weight, with/without watering system). wbSAR normalized to the net RF input power.

Watering System	Antenna configuration				
	Discone		Horn	U-Dipole	
	LOS	NLOS		LOS	NLOS
Absent [19]	3.03 dB	3.06 dB	4.56 dB	3.97 dB	2.48 dB
Present	3.30 dB	3.55 dB [19]	5.26 dB	3.60 dB	2.84 dB

TABLE 5. Probe configuration sweep parameters.

N_U	$\lvert\mathcal{C}_{loc}\rvert$	$\lvert\mathcal{P}_{type}\rvert$	N_{config}
2	66	4	264
4	495	16	7920
6	924	64	59136

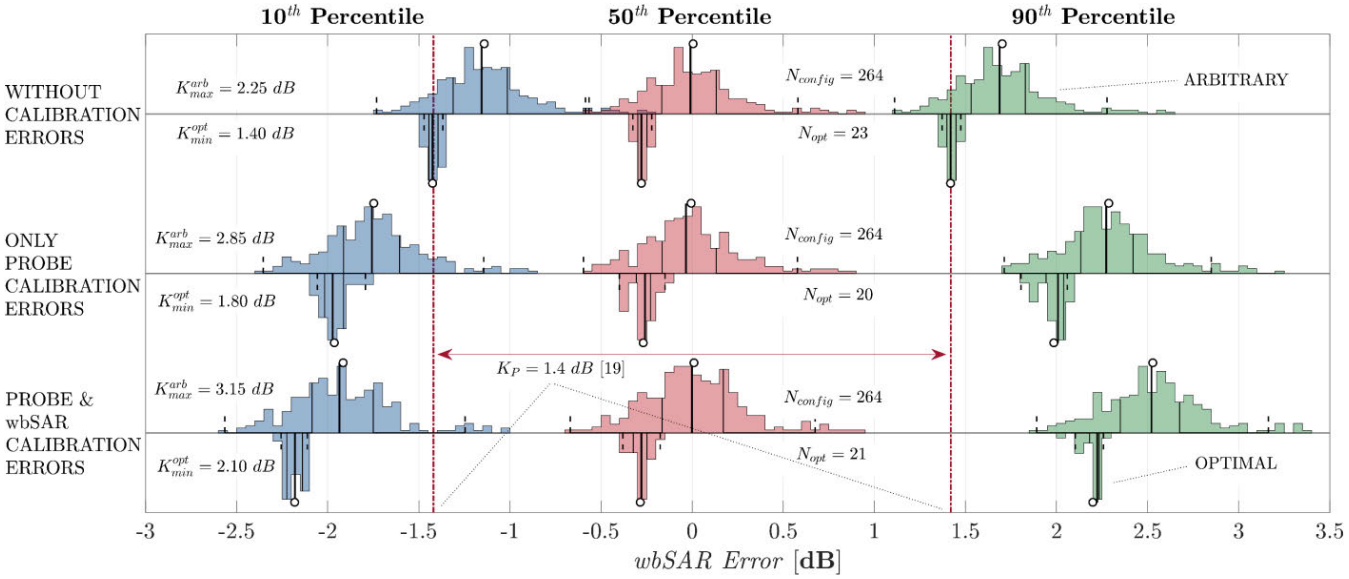

FIGURE 6. Mirrored histograms showing the progression of cohort-wide relative RF-dose errors from the power-normalized spread (K_P) [19] to the case without errors (top) and the cases including probe (middle) as well as the wbSAR calibration errors (bottom), generated by *arbitrary* (upper histograms) versus N_{opt} *optimal* (lower histograms) probe configurations ($N_U = 2$; $N' = N = 96$). RC arrangement with the U-dipole NLOS antenna setup, 650 g mean cohort weight, and the watering system. All values rounded to 0.05 dB. Executing the *control* MC yields the overall median (red) and the probabilistically bounded extreme RF-dose errors: minimum cage-wise 10th percentile (blue) and maximum cage-wise 90th percentile (green) across the $N_{cal} \times N_{live}$ realizations. Within each histogram, thick solid vertical lines indicate the median, thin solid lines denote the IQRs and thin dashed lines represent Tukey's whiskers. Round dots mark the individual distribution means, which align well with the medians in all histograms, indicating minimal skewness. Notably, the gradual widening of the dosimetric error spread occurs across both *arbitrary* and *optimal* probe configurations in this example, making it unrecoverable.

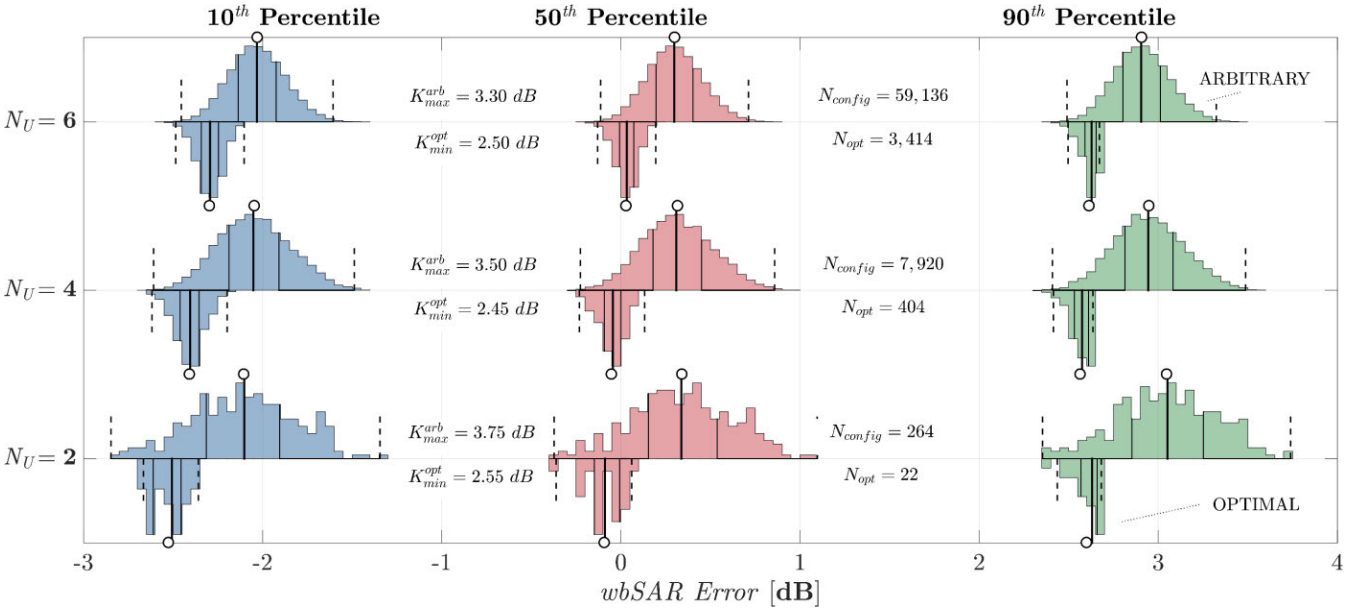

FIGURE 7. Mirrored histograms comparing cohort-wide RF-dose errors generated by *arbitrary* (upper histograms) versus N_{opt} *optimal* (lower histograms) probe configurations, for $N_U = 2, 4$, and 6 field sensors over $N_P = 12$ probing locations ($N' = N = 96$). RC arrangement: discone NLOS antenna setup, 650 g mean cohort weight, watering system. Histogram descriptions, styles, and statistical markers follow those detailed in Fig. 6. Increasing the number of sensors from 2 to 6 yields an approximate 0.5 dB reduction in the one-sided spread for the *arbitrary* probe configurations (K^{arb}_{max}; see also Table 6). Conversely, the absence of improvement for the *optimal* probe configurations (K^{opt}_{min}) reveals a fundamental bound in the achievable RF-dose tightness.

ten subjects within each tail of the distribution. Percentiles further out in the tails (e.g., 95% or 99%) provide an expanded bounding envelope.

Table 5 reports the sweep parameters employed in the following. For each swept probe configuration, the *control* MC engine emulates $N_{cal} = 20$ distinct calibrations, each governing $N_{live} = 20$ independent experiments, totaling 400 MC runs drawing from the stochastic parameters detailed in Table 3. All resulting DFs are evaluated using the arithmetic mean aggregations defined in (5)-(6).

B. RF-DOSE SPREAD FACTOR

Across all studied RC arrangements [17], [18], [19], the observed cohort-wide wbSAR spread falls consistently within a log-symmetric interval like $[1/K, K] \times \text{wbSAR}_{target}$, where the *spread factor* $K > 1$ suitably ranks different RC setups in terms of RF-dose tightness. In the absence of an historically established optimization criterion, probe configurations are assumed to be drawn arbitrarily from the available pool. Accordingly, a conservative figure of merit, denoted K^{arb}_{max}, is defined as the maximum spread factor, which bounds the global exposure minimum of the cage-wise 10th percentiles and the global maximum of the 90th percentiles across all probe configurations. Increasing N_P beyond the 12 current locations would capture wider dosimetric spreads under this arbitrary-choice paradigm.

C. RF-DOSE CONTROL VIA OPTIMAL PROBE SELECTION

As noted in Section II-D, when the live-experiment wbSARs become regulated via (8), their dependency on a specific probe configuration and the associated reading errors locks in, propagating into (11) thus impacting the realized rodent exposures. Hence, the selection of the probe configuration plays a pivotal role in the eventual dosimetric spread. To reduce the spread associated with arbitrary probe selection, a set of optimal probe configurations is obtained by filtering out those featuring $K > K^{opt}_{max}$, progressively increasing such a threshold until a predefined share (e.g., 5%) of all available configurations falls within the range $\left[1/K^{opt}_{max}, K^{opt}_{max}\right] \times wbSAR_{target}$. Setting this quota provides downstream design flexibility to select a practical probe setup. The best configuration in this optimal set corresponds to the lowest spread factor, $K^{opt}_{min} < K^{opt}_{max}$. To exclude outliers, K^{arb}_{max} and K^{opt}_{min} will be derived from Tukey boxplot whiskers, using dB-scale interquartile ranges (IQRs) due to a manifest log-scale symmetry of the respective error distributions.

The foregoing *K-factor filtering* (*KFF*) is illustrated in Fig. 5 for the case of sparse ($N_U = 4$) monitoring probes within the discone NLOS setup. Sweeping the entire configuration ensemble (top histograms), the realized spread factors exhibit a broad distribution spanning $2.40 - 3.60$ dB ($2.80 - 3.45$ dB for the far-probe configurations) with $K^{arb}_{max} = 3.5$ dB (3.45 dB for far probes). *KFF* yields the respective optimal configurations (inverted bottom histograms) capped at ≈5% and ≈20% of the available ones, respectively, with $K^{opt}_{min} = 2.45$ dB (2.80 dB for far probes). Hence, *KFF* bounds the RF-dose range for a given set of probe locations, while providing ample design flexibility. For this RC arrangement, Fig. 5 clearly demonstrates that limiting the choice exclusively to far probes would prove inherently suboptimal.

TABLE 6. Potential cohort-wide dosimetric spread reduction (Δ) for arbitrary and optimal probe configurations across RC arrangements (650g mean cohort weight) [a,b,c].

Antenna		Watering System	Probes Included	$N_U = 2$			$N_U = 4$			$N_U = 6$		
Element	Position			K_{max}^{arb}	K_{min}^{opt}	Δ	K_{max}^{arb}	K_{min}^{opt}	Δ	K_{max}^{arb}	K_{min}^{opt}	Δ
Discone	NLOS	Absent	All	3.25 dB	2.25 dB	1.00 dB	3.00 dB	2.20 dB	0.80 dB	2.90 dB	2.15 dB	0.75 dB
			Far only	*3.25* dB	2.25 dB	1.00 dB	*3.00* dB	2.25 dB	0.75 dB	2.90 dB	2.20 dB	0.70 dB
		Present	All	3.75 dB	2.55 dB	1.20 dB	3.50 dB	2.45 dB	1.05 dB	3.30 dB	2.50 dB	0.80 dB
			Far only	3.60 dB	2.75 dB	0.85 dB	3.45 dB	2.85 dB	0.60 dB	*3.30* dB	2.90 dB	0.40 dB
	LOS	Present	All	3.50 dB	2.40 dB	1.10 dB	3.35 dB	2.30 dB	1.05 dB	3.20 dB	2.30 dB	0.90 dB
			Far only	3.45 dB	2.50 dB	0.95 dB	3.35 dB	2.40 dB	0.95 dB	3.15 dB	2.55 dB	0.60 dB
U-Dipole	NLOS	Present	All	3.15 dB	2.10 dB	1.05 dB	2.90 dB	2.10 dB	0.80 dB	2.75 dB	2.10 dB	0.65 dB
			Far only	3.00 dB	2.20 dB	0.80 dB	2.80 dB	2.10 dB	0.70 dB	2.60 dB	2.15 dB	0.45 dB
	LOS	Present	All	3.60 dB	2.55 dB	1.05 dB	3.45 dB	2.45 dB	1.00 dB	3.30 dB	2.45 dB	0.85 dB
			Far only	3.50 dB	2.65 dB	0.85 dB	3.35 dB	2.50 dB	0.85 dB	3.20 dB	2.65 dB	0.55 dB
Horn	LOS	Present	All	5.40 dB	3.90 dB	1.50 dB	5.10 dB	4.00 dB	1.10 dB	5.00 dB	4.05 dB	0.95 dB
			Far only	5.25 dB	4.25 dB	1.00 dB	5.05 dB	4.25 dB	0.80 dB	4.80 dB	4.35 dB	0.45 dB

([a]): The results for the "Far only" probe configurations exclude the four probes near the back wall and the two midplane probes closest to the stirrer (Fig. 1).

([b]): K_{max}^{arb} and K_{min}^{opt} represent the largest (*arbitrary* selection) and smallest (*optimal* selection) dosimetric spreads, based on higher and lower Tukey's whiskers, respectively, rounded to the nearest 0.05 dB. Optimal selections are based on $\gtrsim$ 5% of all probe configurations and $\gtrsim$ 20% of the far-probe configurations.

([c]): To avoid statistical artifacts, the Tukey's whiskers (K_{max}^{arb} and K_{min}^{opt}) for each dataset are capped at their respective absolute maximum and minimum values, while the italicized values were capped at the Tukey's whisker for all configurations since a "Far only" subset cannot expand wider than the full dataset.

D. ERRORS IMPACT ON DOSIMETRIC SPREAD

In [19, Table 7], normalizing the simulated wbSAR results to the net RF input power in the absence of calibration errors induced slightly tighter dosimetric spreads than normalizing with respect to the electric or the total RF energy densities (both aggregated over the full 12-probe configuration). Here, that analysis is expanded by quantifying the RF-dose spread across arbitrary or optimal probe configurations rather than the full 12-probe setup, and by corrupting probe readings and thermal wbSAR estimates with realistic calibration errors.

1) ERRORS INJECTED WITHIN THE DOSIMETRIC EMULATION

Table 5 in [4] breaks down the "exposure field uncertainty" into six root-sum-squared (RSS) components. Of these, four (absolute accuracy, frequency and dynamic range linearities, and isotropy) pertain to the individual $\boldsymbol{E}$- or $\boldsymbol{H}$-field sensors; upon correcting a clerical error in the isotropy row, they combine to yield a 9.1% overall probe reading R-SD.

Table 5 in [14] comprises three error components (field control, RC temperature fluctuations, and temperature probe readings) impacting cohort-wise mean wbSAR estimates during calibrations. Since temperature sensors probed every liquid-filled bottle during the NTP rat bioassay calibrations, the emulated calibration MC engine features a cage-wise raised-cosine error injection with an 11.8% R-SD, yielding the 1.2% standard percentile error figure reported in [14] upon averaging across 96 phantoms. This component is indeed marginal within the overall error budget, as the rest combine quadratically to yield a 10.7% R-SD (Table 3).

2) ERROR-DRIVEN RF-DOSE SPREAD FOR THE U-DIPOLE NLOS

Figure 6 illustrates the RF-dose error spread for an RC arrangement featuring the U-dipole NLOS setup, the watering system, and $N_U = 2$ out of $N_P = 12$ probe locations ($N_{config} = 264$, Table 5). A steady degradation of the cage-wise exposure tightness is clearly shown over subsequent mirrored histograms of the realized RF-dose minima (10th percentile, blue), medians (red), and maxima (90th percentile, green), presented in a dB scale relative to the target. In the top histograms, under hypothetical, error-free conditions, the transition from a global normalization quantity (net RF input power) to discrete spatial sampling inherently widens the RF-dose spread due to the RC field spatial inhomogeneities. The spread factor $K_P = 1.4\ dB$ in Fig. 6 represents half the most extreme range (i.e., 0th to 100th percentile) in Table 4 for the power-normalized U-dipole NLOS setup (watering system present). Absent calibration errors, over the tracked 10th-to-90th percentile range, the optimal probe selections substantially offset discrete-sampling spread. However, as seen in the middle and bottom histograms, injecting realistic calibration errors steadily degrades the dosimetric spread for arbitrary probe configurations and, remarkably, the optimal selections can no longer restore the error-free tightness, indicating that calibration-error-driven spread is irreversible.

E. PROBE NUMBER IMPACT ON DOSIMETRIC SPREAD

The results presented in III-D clearly illustrate the inevitable, progressive, unrecoverable loss of RF-dose tightness caused by the compounded effect of sparse RC-field sampling and ineluctable calibration errors. Here, the impact of increasing the number of probing locations is quantified with reference to the RC arrangement featuring the discone NLOS setup with the watering system, which is the most representative in terms of dosimetric spread (Table 4).

Over an increasing number of field probing locations ($N_U = 2, 4, 6$; $N_P = 12$), the mirrored histograms in Fig. 7 depict the respective cage-wise RF-dose ranges when the net RF input power is regulated by all the available probe configurations (*upper* histograms) and their optimal subsets

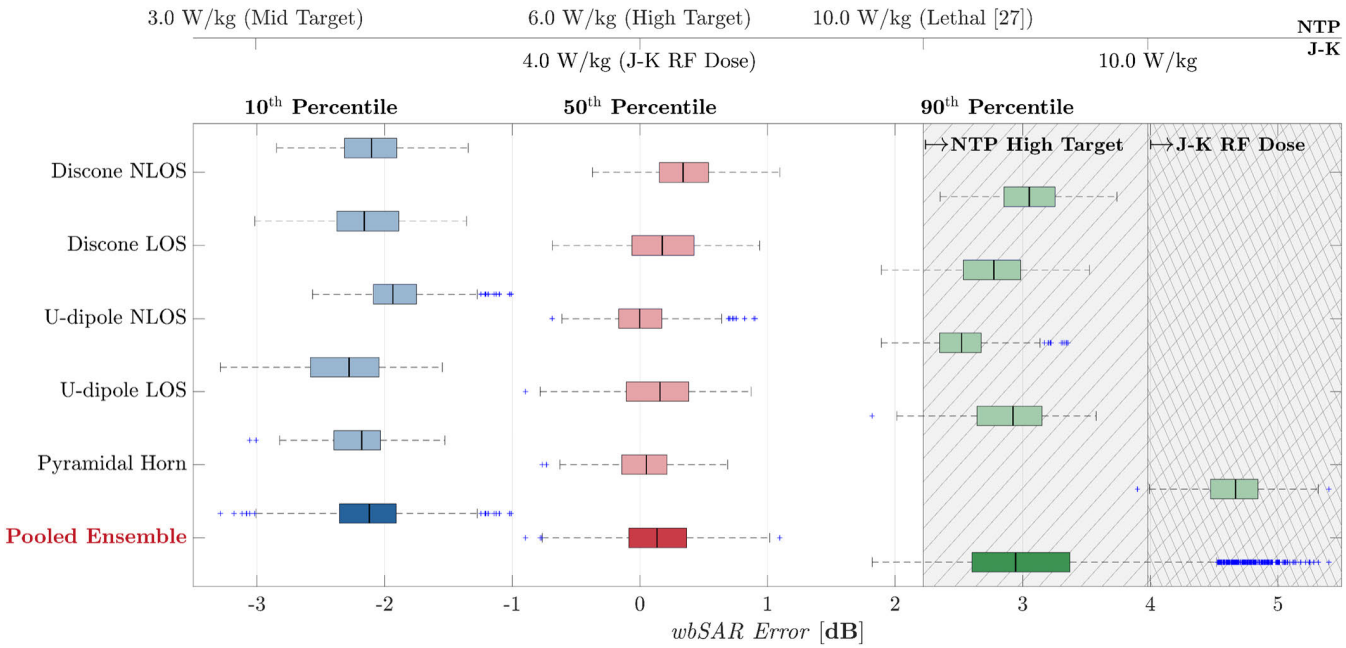

FIGURE 8. Tukey's boxplots describing the dosimetric spread of the realized cage-wise exposures across antenna setups, in terms of the minimum 10th percentile (blue), median (red), and maximum 90th percentile (green) over $N_{cal} \times N_{live}$ live-experiment MC realizations run for each arbitrary dual-probe configuration ($N_U = 2, N_{config} = 264$). The upper axis contextualizes these dosimetric errors relative to the 6.0 W/kg high-dose target adopted in the NTP rat bioassay, as well as relative to the hypothetical adoption of the 4.0 W/kg Japan-Korea (J-K) partial replication target [10]. Shaded regions illustrate how unmitigated variance may induce dose-group overlaps or drive exposures above potentially lethal levels (i.e., surpassing the 10 W/kg threshold documented in [27]). The long-tailed 90th percentile spread in the pooled ensemble underscores the outlier behavior of the pyramidal horn antenna.

(*lower* histograms, see Section III-C). Analogous to Fig. 6, arbitrary probe configuration choices lead to severe dose spreads.

For this RC arrangement, 264 arbitrary dual-probe configurations yield broad, stretched profiles with maximum exposure bounds exceeding 3 dB (twice the target dose) for the 90th percentile dataset, indicating that in practice several cages out of 96 may experience similar overexposure.

Increasing the sensor count to 4 or 6 arbitrary probes yields limited benefit; while the median IQRs compress slightly, the overall RF-dose spread remains wide and skewed high, underscoring the challenge of mitigating this inherent variance. For the optimal subsets, in contrast to the full-set baseline, the higher dosimetric tails are truncated as the cohort-wide maxima are pushed lower, improving the overall RF-dose tightness. However, even with 6 probes, the two-sided baseline range using net RF power normalization (3.55 dB, Table 4; i.e., $K_P \approx 1.8\ dB$) could not be attained. Limiting the selection to the far probes yields diminishing returns; by the time $N_U = 6$, the only degrees of freedom left are the 64 probe-type permutations.

F. RF-DOSE SPREAD ACROSS RC ARRANGEMENTS

The *KFF*-based selection was applied to the structural RC arrangements listed in Table 4, evaluating various antennas and N/LOS placements. A high-directivity pyramidal horn antenna, which may inject significant unstirred energy into heavily loaded cavities, was deliberately compared with two low-gain radiators (discone and U-dipole [17]) to exacerbate spatial energy gradients across the cohort volume, widening the cage-wise exposure imbalances ([19], Table 6).

All cases included the intrusive watering system; to isolate this effect, the discone NLOS setup was also characterized without it. Moreover, the probe configuration analysis was split to allow choosing from either all N_P probing locations or only the six distal "far probes" indicated in Fig. 1. Narrowing the choice tightens the worst-case range as fewer degrees of freedom exist to yield suboptimal configurations; however, such a restriction inherently undermines the attainable RF-dose tightness with optimal probe selections.

Table 6 summarizes the cohort-wide RF-dose spreads across RC arrangements using $N_U = 2, 4,$ or 6 field probes. The *one-sided* wbSAR spread reduction (Δ) is quantified, as in Figs. 5 and 6, by the dB-difference between widest arbitrary-probe (K_{max}^{arb}) and narrowest optimal-probe spreads (K_{min}^{opt}). The overall spread reduction is 2Δ dB. Clearly, *KFF* consistently shrinks the exposure spread by around 1 dB (one-sided), with smaller reductions observed at $N_U = 6$. Notably, the pyramidal horn yields the largest reductions, albeit from the widest initial spreads, as its high directivity exacerbates probed-field dominance in highly loaded RCs [19]. This finding underscores the need for rigorous experimental validation prior to bioassay deployment of high-gain radiators in heavily loaded RCs.

As anticipated, restricting the analysis to distal probes lowers the baseline K_{max}^{arb} and inherently narrows the attainable improvements. However, such a small K_{max}^{arb} contraction renders this restriction ineffectual. While standard guidelines

TABLE 7. Chronological comparison of computational dosimetry frameworks for RC-based rat bioassays.

Study (Year)	Computational Model & Field Representation	RC Infrastructure & Loading Scope	Exposure Control Metric	Exposure Granularity	Key Results	Limitations & Physical Bounds
Capstick *et al.* (2017) [4]	FDTD 12-PW superposition (6 directions x 2 polarizations)	Heterogeneous rat models; water sipper coupling;	Unregulated incident field (1 V/m)	Single-cage analysis; sipping rats; wbSAR dependency on mass; organ SAR	Study frequency association with rodent species; sipper currents	Single-cage wbSAR; error propagation analysis extended to the cohort-mean (no cage-wise histograms)
Gong *et al.* (2017) [14]	FDTD 12-PW superposition (6 directions x 2 polarizations)	Heterogeneous & homogeneous rat models; discrete masses & postures	Unregulated incident field (1 V/m)	Single-cage analysis; mean RF dose across mass groups; organ SAR	Life-time wbSAR and organ SAR across mass and discrete postures	Single-cage wbSAR; error propagation analysis extended to the cohort-mean (no cage-wise histograms)
Jeon *et al.* (2021) [5]	FDTD 52-PW superposition (26 directions x 2 polarizations)	Heterogeneous rat models (527 g)	Unregulated incident field (1 V/m)	27-rat cohort-wide wbSAR mean and standard deviation;	wbSAR vs. distance b/w rats; optimal cage distance	52-PW spatial correlation at most $1.2\lambda_0$ [13]; fixed weight & single posture
Ito *et al.* (2022) [7]	FDTD 52-PW superposition (26 directions x 2 polarizations)	Heterogeneous rat models; pup to adult stages; watering pipes	Unregulated incident field (1 V/m)	Stage-averaged cohort wbSAR; rat orientation; 2D wbSAR model vs mass and number of rats	Field uniformity; multi-stage wbSAR cohort-mean & uncertainty	Free-space PWs; Open-loop, unperturbed incident fields; omits cage-wise SAR spread and organ SAR analysis
De Santis *et al.* (2023) [16]	FDTD 5000 PWs (spiral-distributed incidence [13], elliptically polarized)	Homogeneous rat models; random posture, position, orientation, mass (650g ≈12% R-SD)	Unregulated incident field squared (5000 V^2/m^2)	MC-based 96-rat wbSAR cohort-mean, R-SD; wbSAR cage-wise spread & cage-position impact; wbSAR-mass correlation	Small cage position impact on wbSAR; wide lognormal instantaneous wbSAR spread	Free-space PWs; Open-loop, unperturbed incident fields; no watering pipe or antenna effects (high vs. low gain, LOS vs. NLOS placement)
Faraone *et al.* (2026) [19]	TLM Full-Wave RC digital twin (UNIVPM-RC with large stirrer)	Models as in [16]; grounded watering system, choked sippers; high and low-gain antennas	Open-loop net RF input power at antenna feed	MC results as in [16] & cage assembly rotational or translational dynamics; ensemble impedances & probe dominance scores;	Cage-wise wbSAR imbalance; wbSAR-mass correlation; spread reduction via rotational dynamics	Open-loop exposures; High Power Computing (HPC) resources (TLM & GPUs); no wbSAR imbalances due to empty cages (early deaths)
This Work	TLM Full-Wave RC digital twin (UNIVPM-RC with large stirrer & 12 field probes)	Live-experiment models as in [19]; fixed posture/mass calibration models; no cage dynamics	Latency & drift free closed-loop net RF-power control through RC field sensing	Nested MCs yielding calibration & field sensor error propagation impact on 10^{th} & 90^{th} percentile cage-wise wbSAR	Calibration-to-live experiment error-driven wbSAR spread; optimal probe selection	HPC; optimistic assumptions on exposure control, without environmental effects or wbSAR imbalances due to empty cages (early deaths)

(e.g., [26]) dictate a minimum clearance between field probes and RC structures, *KFF* leverages the entire RC volume, including commonly neglected locations, to yield optimal RF-dose spreads as in Fig. 7.

Ultimately, *KFF* represents a practical and robust tool for regulating localized exposures, offering the flexibility to deploy probes near RC structures, which may prove advantageous in compact RC designs.

IV. DISCUSSION

To provide consequential context for the dosimetric variances detailed in Section III, the emulation framework results can be mapped to historical large-scale bioassay parameters [4], [5], [6], [7] (Table 7 summarizes chronologically the underpinning computational RC dosimetry). Notably, Appendix B shows that the fading characteristics of the loaded UNIVPM-RC digital twin align well with ideal Rayleigh fading, making its use acceptable in the context of historical bioassays; any significant deviation from well-stirred fields in actual RCs, degrading the exposure field uniformity, would plausibly amplify the dosimetric spread reported here.

Historically, exposure groups typically follow a geometric target progression (e.g., the 1.5, 3.0, and 6.0 W/kg RF dose targets in the NTP rat bioassay [8]) to attain sufficient inter-group RF-dose separation for assessing potential dose-response links reliably (the limited J-K replication featured a single 4.0 W/kg target [10], [11]). Preventing overexposures mitigates the potential for biophysical responses that might subsequently confound the bioassay interpretation. Of note, thermal pilot studies associated with the NTP rodent bioassays determined that whole-body exposures approaching 10 W/kg would induce lethal thermal loads in aged rats [27]. These studies evaluated young and aged male rats, with the latter averaging 470 g (CDMA waveform) and 504 g (GSM), significantly less than the 650 g plateau attained by adult male rats in the main bioassay [8]. Due to a higher body volume-to-surface ratio, adult rats exhibit lower heat-dissipation capacity than the aged rats, which failed to survive 24 h above 10 W/kg. At such levels, even under the intermittent 10-minute on-off exposure paradigm [8], maintaining a homeostatic core body temperature could present a severe physiological challenge. Physiological stress biomarkers (e.g., corticosterone) were not tracked in the NTP bioassays or the J-K replication.

Contextualized within the parameters of the NTP male rat bioassay, Figure 8 illustrates the statistical RF-dose spreads across the antenna setups for arbitrary dual-probe monitoring configurations. By centering the respective dosimetric spread at the high-dose NTP target (6.0 W/kg), the boxplots describe the realized cage-wise error distributions for the statistical descriptors introduced in Figs. 5 and 6, across all 264 available probe configurations (no *KFF* mitigation). The implications of this unmitigated variance are twofold:

- Overlap: the inter-group dosimetric separation appears compromised, as a deviation greater than ± 1.5 *dB* causes overlaps between adjacent dose tiers, which would occur in Fig. 8 for every antenna setup. A significant proportion of animals in a given exposure group would fall outside its bounds, presenting a potential dose-response confounder.
- Overexposure: all the 90^{th} percentile error distributions fall almost entirely within the reported lethal range [27], sitting only ≈ 2 *dB* above the high-dose target, indicating that excessive thermal stress cannot be ruled out.

Regarding the last point, Fig. 8 also maps a counterfactual scenario adopting the 4.0 W/kg J-K RF-dose target, pushing the associated lethal threshold to ≈ 4 *dB*. Only the outlier pyramidal horn setup would fall in that range. Note that the present analysis is not otherwise applicable to the J-K replication due to differing parameters.

Ultimately, without an *a priori* optimal probe selection to inform the bioassay RF-dose target settings, an arbitrarily monitored live experiment may unknowingly induce thermal stress in rodents, confounding outcome interpretations.

Beyond the immediate magnitude of RF-dose errors, it is important to recognize their systemic and structural nature. The results of this study demonstrate that the wbSAR spread introduced by arbitrary probe configurations and dosimetric calibration errors is unrecoverable. Selecting an arbitrary probe arrangement structurally locks in the global controller bias in (11), while probe calibration errors lock in their respective responses for weeks or months between calibration cycles. Furthermore, the cage-wise RF-dose bias in (11) results in permanent thermal load imbalances, as the relative cage-to-cage exposure ranking is inherently set. These physical realities remain entirely unobserved by the controller: hidden confounders that do not average out.

Finally, in assessing the broader implications of this study, recall that the dosimetric analysis was intentionally carried out under a fairly optimistic scenario, neutralizing potential confounders by design. Factors such as lifelong animal growth, unpredictable postural shifts, and environmental changes may further inflate the RF-dose spread. Given recent findings that heavier rodents lack proportional thermal "mass buffering" in heavily loaded RCs, future bioassay designs should prudently account for all known or anticipated error sources when establishing target exposure bounds. Future developments may include the integration of real-time computer vision and adaptive dosimetric models to support RF-power control and reduce dosimetric variability in long-term bioassays. Securing wireless control telemetry against tampering would then become even more pressing.

V. CONCLUSION

This study narrows the gap between idealized random PW exposure models and the physical and operational reality of an actual rodent-loaded RC. Unlike prior PW models that omit boundary coupling [16] or open-loop digital twins that ignore controller feedback [19], the proposed closed-loop framework captures relevant error propagation. Building upon cross-validations of FEM and TLM simulations of a realistic loaded RC digital twin [17], [18], and the findings on dose-mass correlation and exposure imbalances in a heavily loaded RC [19], an MC-based granular dosimetric analysis, involving the emulation of plausible calibration-to-bioassay scenarios, is presented. The results document a steady erosion of certainty in the RF dose, expressed in terms of ensemble-averaged wbSAR, where the dosimetric spread widens as the regulated exposure shifts from macroscopic control metrics (input power) to spatially discrete ones (field probe readings), and gradually widens further upon accounting for systematic instrumentation errors. Increasing the number of probes yields limited benefits, as these errors set a fundamental bound to the attainable RF-dose tightness. From a facility design standpoint, KFF provides a traceable method to optimize probe locations *a priori*, without cluttering the RC with excessive sensor hardware. For the UNIVPM-RC digital twin, KFF yields a ≈ 1 dB cage-wise wbSAR spread reduction for a given antenna configuration and up to ≈ 3 dB across antennas.

The results were mapped onto the parameters of the NTP rat bioassay [8] to assess whether relying on arbitrary sparse

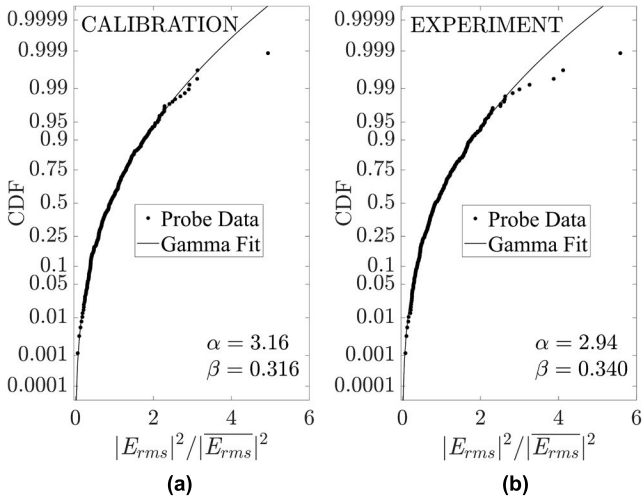

FIGURE 9. Gamma distribution fits of the empirical, mean-normalized ($\alpha\beta = 1$) squared *rms E*-field magnitude CDFs for the baseline RC arrangement (discone NLOS; watering system; 650 g mean weight): (a) calibration and (b) live experiment phase emulations. The close agreement between the fitting curves (solid lines) of the sampled fields (dots) and the theoretical χ^2_6 distribution, corresponding to a gamma distribution with a shape parameter $\alpha = 3$, indicate well-stirred fields for the UNIVPM-RC digital twin.

dual-probe configurations might cause dose-group overlaps or significant overexposures, potentially complicating the toxicological interpretation. Even under benign assumptions, this analysis illustrates how sparse field-sampling and the inherent experimental errors compound to cause significant RF-dose spread, quantifying the potential exposure group overlaps and overexposures.

Ultimately, since instrumentation errors are ineluctable, achieving tighter RF-dose control hinges on the *a priori* selection of optimal probe configurations informed by high-fidelity RC digital twins. Hence, granular and statistically thorough estimates of realistic RF-dose spreads will be critical in the design of bioassay equipment and protocols. To that end, compared with earlier PW or open-loop frameworks, the proposed closed-loop architecture advances RC dosimetry by emulating calibration-to-live experiment chronology, tracking error propagation while optimizing probe selection to bound the cohort RF-dose spread. Due to the required HPC resources, the associated computational burden represents a principal practical trade-off.

APPENDIX A
TOTAL RF ENERGY REGULATING LAW

When the total RF energy density is used to regulate the RF-dose control loop, adopting a weighted average of the fractional electric and magnetic energy error estimates presents some practical advantages. The distinct calibration uncertainty of different probe types can be taken into account by increasing the relative weight of the more accurate type. Moreover, this approach normalizes the feedback control signal across exposure tiers, avoiding the need to retune controller sensitivity for different targets. Finally, it prevents conferring excessive weight to whichever field happens to dominate (e.g., per the field-dominance scores in [19]).

Denoting with v_E and v_H the R-SDs of $\boldsymbol{E}$-field and $\boldsymbol{H}$-field probe calibrations, respectively, the aggregate fractional error is defined in terms of error-laden metrics as:

$$\delta_U^{err} = \frac{1}{v_E^2}\frac{N_E}{N_U}\frac{\left\langle \widetilde{\Psi_E^{live}} \right\rangle - \left\langle \widetilde{\Psi_E^{cal}} \right\rangle_{target}}{\left\langle \widetilde{\Psi_E^{cal}} \right\rangle_{target}} + \frac{1}{v_H^2}\frac{N_H}{N_U}\frac{\left\langle \widetilde{\Psi_H^{live}} \right\rangle - \left\langle \widetilde{\Psi_H^{cal}} \right\rangle_{target}}{\left\langle \widetilde{\Psi_H^{cal}} \right\rangle_{target}}, \tag{A1}$$

where $\left\langle \widetilde{\Psi_E^{cal}} \right\rangle_{target}, \left\langle \widetilde{\Psi_H^{cal}} \right\rangle_{target}$ yield $\left\langle \widetilde{\Psi_U^{cal}} \right\rangle_{target}$ via (2).

As the feedback-control loop drives the fractional error (A1) to zero by manipulating in real-time the net RF input power, which is proportional to both $\left\langle \widetilde{\Psi_E^{live}} \right\rangle$ and $\left\langle \widetilde{\Psi_H^{live}} \right\rangle$, the following global controller bias stems from (5)-(6):

$$\frac{\widetilde{\mathrm{wbSAR}}_{live}}{\mathrm{wbSAR}_{target}} = \frac{\frac{N_E}{v_E^2} + \frac{N_H}{v_H^2}}{\frac{N_E}{v_E^2}\frac{\widetilde{\mathrm{DF}}_E^{cal}}{\widetilde{\mathrm{DF}}_E^{live}} + \frac{N_H}{v_H^2}\frac{\widetilde{\mathrm{DF}}_H^{cal}}{\widetilde{\mathrm{DF}}_H^{live}}}. \tag{A2}$$

Evidently, this expression yields (9) if $N_E = 0$ or $N_H = 0$. It is always possible to drive δ_U^{err} to zero, even though the factors κ_E, κ_H inherently linking $\left\langle \widetilde{\Psi_E^{live}} \right\rangle, \left\langle \widetilde{\Psi_H^{live}} \right\rangle$ to the net RF input power shift with the dynamic RC loading, as δ_U^{err} depends linearly on the incident RF power (P_{inc}):

$$\delta_U^{err} = \frac{\left(1 - |\Gamma_A|^2\right) P_{inc}}{N_U}\left(\frac{N_E \frac{\kappa_E}{v_E^2}}{\left\langle \widetilde{\Psi_E^{cal}} \right\rangle_{target}} + \frac{N_H \frac{\kappa_H}{v_H^2}}{\left\langle \widetilde{\Psi_H^{cal}} \right\rangle_{target}}\right) - \frac{\frac{N_E}{v_E^2} + \frac{N_H}{v_H^2}}{N_U}. \tag{A3}$$

Therefore, a classic Proportional-Integral-Derivative (PID) controller, or a memory-less, regularized control scheme tailored to a specific RC design (as in [28]), can enforce compliance $\left(\left\langle \delta_U^{err} \right\rangle \to 0\right)$ without instability even if the antenna reflection coefficient (Γ_A) is not monitored.

While the zero-latency, drift-free control in the proposed MC framework neglects transient delays, inertia, and non-linear tracking errors typical of PID hardware, any transient fluctuations in a practical PID loop would average out over a significantly faster timescale than the rodents thermophysiological response. Barring undetected hardware drifts over time, their physiological impact should be negligible.

APPENDIX B
UNIVPM-RC DIGITAL TWIN RF FADING STATISTICS

To validate the stirring effectiveness of the UNIVPM-RC digital twin, the empirical distributions of the sampled fields at the 12 probing locations in Fig. 1 were benchmarked against theoretical Rayleigh fading characteristics [29]. In an ideal, well-stirred RC operating in an overmoded regime, the squared magnitudes of the fields across a sufficiently large number of stirrer positions follow respective χ_6^2 distributions (two degrees of freedom for each squared field component). The χ_6^2 distribution coincides with the gamma distribution having shape parameter $\alpha = 3$ [16]. As shown in Fig. 9 for the baseline RC arrangement (discone NLOS setup with the watering system, 650 g mean weight), the empirical CDFs of the sampled fields, for the calibration and live experiment simulations, yield very close agreement with the Rayleigh fading theory ($\alpha \simeq 3$). Consequently, the dosimetric variances inferred from the UNIVPM-RC digital twin are sufficiently representative of the high-quality RC facilities utilized in landmark bioassays.

ACKNOWLEDGMENT

The authors would like to acknowledge Dr. John Osepchuk (1927–2024), IEEE Life Fellow, for his input to the IEEE International Committee on Electromagnetic Safety (ICES) on the significance of granular RF-dose statistical descriptors to quantify dosimetric spreads in loaded RCs.

REFERENCES

[1] K. B. Jung, T. H. Kim, J. L. Kim, H. J. Doh, Y. C. Chung, J. H. Choi, and J. K. Pack, "Development and validation of reverberation-chamber type whole-body exposure system for mobile-phone frequency," *Electromagn. Biol. Med.*, vol. 27, no. 1, pp. 73–82, Mar. 2008.

[2] J. Shi, J. Chakarothai, J. Wang, K. Wake, S. Watanabe, and O. Fujiwara, "Quantification and verification of whole-body-average SARs in small animals exposed to electromagnetic fields inside reverberation chamber," *IEICE Trans. Commun.*, vol. E97.B, no. 10, pp. 2184–2191, Oct. 2014. [Online]. Available: https://www.jstage.jst.go.jp/article/transcom/E97.B/10/E97.B_2184/_article/-char/en

[3] C. Li, L. Yang, B. Lu, Y. Xie, and T. Wu, "A reverberation chamber for rodents' exposure to wideband radiofrequency electromagnetic fields with different small-scale fading distributions," *Electromagn. Biol. Med.*, vol. 35, no. 1, pp. 30–39, Jan. 2016.

[4] M. Capstick, S. Kuehn, V. Berdinas-Torres, Y. Gong, P. F. Wilson, J. M. Ladbury, G. Koepke, D. L. McCormick, J. Gauger, R. L. Melnick, and N. Kuster, "A radio frequency radiation reverberation chamber exposure system for rodents," *IEEE Trans. Electromagn. Compat.*, vol. 59, no. 4, pp. 1041–1052, Apr. 2017.

[5] S. Jeon, W. Jang, A.-K. Lee, H.-D. Choi, J.-K. Pack, J. Wang, and D. Kim, "Distances between rats in reverberation chambers used for large-scale experiments," *J. Electromagn. Eng. Sci.*, vol. 21, no. 2, pp. 148–152, Apr. 2021.

[6] S. Jeon, A.-K. Lee, J. Wang, J.-K. Pack, Y.-B. Kim, Y. H. Ahn, K. Imaida, and H.-D. Choi, "Field uniformity assessment of a reverberation chamber for a large-scale animal study," *IEEE Access*, vol. 9, pp. 146471–146477, 2021.

[7] R. Ito, S. Jeon, J. Wang, A.-K. Lee, J.-K. Pack, H.-D. Choi, Y. H. Ahn, and K. Imaida, "Quantification of exposure level in a reverberation chamber for a large-scale animal study," *IEEE J. Microw.*, vol. 2, no. 3, pp. 522–532, Jul. 2022.

[8] The US National Toxicology Program, "NTP technical report on the toxicology and carcinogenesis studies in HSD:Sprague dawley rats exposed to whole-body radio frequency radiation at a frequency (900 MHz) and modulations (GSM and CDMA) used by cell phones," Nat. Toxicol. Program, Research Triangle Park, NC, USA, Tech. Rep. NTP TR 595, 2018.

[9] "NTP technical report on the toxicology and carcinogenesis studies in B6C3F1/N mice exposed to whole-body radio frequency radiation at a frequency (1,900 MHz) and modulations (GSM and CDMA) used by cell phones," Nat. Toxicol. Program, Tech. Rep. NTP TR 596, 2018.

[10] H. S. Kim, K.-H. Han, Y.-B. Kim, S. B. Jeon, A.-K. Lee, J.-I. Moon, H. D. Choi, K. Imaida, M. Yokohira, M. Kawabe, N. Imai, J. Wang, and Y. H. Ahn, "The international collaborative animal study of the carcinogenicity and genotoxicity of mobile phone radiofrequency radiation: The Korean study," *Toxicolog. Sci.*, vol. 209, no. 3, pp. 1–15, Mar. 2026. [Online]. Available: https://academic.oup.com/toxsci/advance-article-pdf/doi/10.1093/toxsci/kfag001/66436794/kfag001.pdf

[11] K. Imaida, M. Kawabe, J. Wang, M. Yokohira, N. Imai, K.-H. Han, Y.-B. Kim, S. B. Jeon, H. S. Kim, and Y. H. Ahn, "The international collaborative animal study of mobile phone radiofrequency radiation carcinogenicity and genotoxicity: The Japanese study," *Toxicolog. Sci.*, vol. 209, no. 3, pp. 1–15, Mar. 2026. [Online]. Available: https://academic.oup.com/toxsci/advance-article-pdf/doi/10.1093/toxsci/kfag002/66382273/kfag002.pdf

[12] *American National Standard Safety Levels With Respect to Human Exposure to Radio Frequency Electromagnetic Fields, 300 KHz to 100 GHz*, Standard ANSI C95.1-1982, 1982.

[13] A. Di Francesco, V. De Santis, G. Bit-Babik, and A. Faraone, "An efficient plane-waves superposition method for improved spatial correlation in simulated reverberation chambers," *IEEE Access*, vol. 10, pp. 119641–119648, 2022.

[14] Y. Gong, M. H. Capstick, S. Kuehn, P. F. Wilson, J. M. Ladbury, G. Koepke, D. L. McCormick, R. L. Melnick, and N. Kuster, "Life-time dosimetric assessment for mice and rats exposed in reverberation chambers for the two-year NTP cancer bioassay study on cell phone radiation," *IEEE Trans. Electromagn. Compat.*, vol. 59, no. 6, pp. 1798–1808, Dec. 2017.

[15] S. Sandeep, A. F. Peterson, and J. Wiart, "Whole body SAR estimation of a rodent inside a reverberation chamber," *J. Electromagn. Waves Appl.*, vol. 39, no. 18, pp. 2426–2445, Dec. 2025.

[16] V. De Santis, A. Di Francesco, K. R. Foster, G. Bit-Babik, and A. Faraone, "Monte-carlo based numerical dosimetry in reverberation chamber exposure systems employed for in-vivo rodent bioassays," *IEEE Access*, vol. 11, pp. 22018–22033, 2023.

[17] A. Faraone, G. Bit-Babik, P. Russo, A. De Leo, V. Mariani Primiani, and V. De Santis, "Computational RF dosimetry of rodents cohorts in a realistic reverberation chambers at 900 MHz," in *Proc. Int. Symp. Electromagn. Compat. – EMC Eur.*, Bruges, Belgium, Sep. 2024, pp. 957–960.

[18] A. Faraone, G. Bit-Babik, K. Sanderson, P. Russo, A. De Leo, V. M. Primiani, and V. De Santis, "Numerical characterization of rodent exposure imbalances in large reverberation chambers," in *Proc. Int. Symp. Electromagn. Compat.*, Paris, France, Sep. 2025, pp. 1103–1107.

[19] A. Faraone, G. Bit-Babik, K. Sanderson, P. Russo, A. de Leo, V. M. Primiani, and V. de Santis, "Full-wave characterization of reverberation chambers for rodent bioassays: Methodology and realistic-loading impact analysis," *IEEE Access*, vol. 14, pp. 74261–74273, 2026.

[20] D. Appicciutoli, G. Buoncompagni, and V. Mariani Primiani, "Experimental activity in using a reverberation chamber for emission and shielding effectiveness measurements: Comparison with traditional deterministic methods," in *Proc. EMC Eur., Int. Symp. Electromagn. Compat.*, Eindhoven, The Netherlands, Sep. 2004, pp. 1–6.

[21] F. Moglie and V. Mariani Primiani, "Numerical simulations of field values, wave impedance, and received power inside a nonideal reverberation chamber," *IEEE Trans. Electromagn. Compat.*, vol. 56, no. 4, pp. 994–997, Aug. 2014.

[22] Q. Balzano, C. Chou, R. Cicchetti, A. Faraone, and R. Y.-S. Tay, "An efficient RF exposure system with precise whole-body average SAR determination for in vivo animal studies at 900 MHz," *IEEE Trans. Microw. Theory Techn.*, vol. 48, no. 11, pp. 2040–2049, Nov. 2000, doi: 10.1109/22.884193. [Online]. Available: https://ieeexplore.ieee.org/document/884193

[23] A. Faraone, W. Luengas, S. Chebrolu, M. Ballen, G. Bit-Babik, A. V. Gessner, M. Y. Kanda, T. Babij, M. L. Swicord, and C.-K. Chou, "Radiofrequency dosimetry for the ferris-wheel mouse exposure system," *Radiat. Res.*, vol. 165, no. 1, pp. 105–112, Jan. 2006.

[24] Y.-S. Shiu, S. Y. Chang, H.-C. Wu, S. C.-H. Huang, and H.-H. Chen, "Physical layer security in wireless networks: A tutorial," *IEEE Wireless Commun.*, vol. 18, no. 2, pp. 66–74, Apr. 2011.

[25] R. Chen, C. Yi, K. Zhu, B. Chen, J. Cai, and M. Guizani, "A three-party hierarchical game for physical layer security aware wireless communications with dynamic trilateral coalitions," *IEEE Trans. Wireless Commun.*, vol. 23, no. 5, pp. 4815–4829, May 2024.

[26] *Electromagnetic Compatibility (EMC)—Part 4-21: Testing and Measurement Techniques-Reverberation Chamber Test Methods*, Standard IEC 61000-4-21:2011, International Electrotechnical Commission, 2011.

[27] M. E. Wyde, T. L. Horn, M. H. Capstick, J. M. Ladbury, G. Koepke, P. F. Wilson, G. E. Kissling, M. D. Stout, N. Kuster, R. L. Melnick, J. Gauger, J. R. Bucher, and D. L. McCormick, "Effect of cell phone radiofrequency radiation on body temperature in rodents: Pilot studies of the national toxicology program's reverberation chamber exposure system," *Bioelectromagnetics*, vol. 39, no. 3, pp. 190–199, Apr. 2018.

[28] D. Izzo, A. Rommel, M. Aidam, R. Vogt-Ardatjew, and F. Leferink, "A cosed-loop calibration method for the vibrating intrinsic reverberation chamber," in *Proc. Int. Symp. Electromagn. Compat.*, Rome, Italy, Sep. 2020, pp. 1–6.

[29] D. A. Hill, "Electromagnetic theory of reverberation chambers," Nat. Inst. Standards Technol., Boulder, CO, USA, NIST Tech. Note 1506, 1998.

ANTONIO FARAONE (Senior Member, IEEE) was born in Rome, Italy, in 1966. He received the Ph.D. degree in applied electromagnetics from the University of Rome "La Sapienza," in 1997. In 1997, he joined the Motorola (later Motorola Solutions) Corporate Electromagnetic Energy (EME) Research Laboratory, Fort Lauderdale, FL, USA, engaging in mobile antenna technology and RF dosimetry research, and IEEE/IEC RF exposure safety and product compliance standards. He is currently the Chief EME Scientist, overseeing product RF exposure compliance. He has co-authored about 45 refereed journal publications and holds 50 patents, mostly in RF and antennas. He is a Motorola Innovators Circle (MIC) Member, a Master Innovator, and a Dan Noble Fellow. He is a member of Italian Society of Electromagnetics (SIEm). He was a recipient of the IEC 1906 Award. He is the Secretary of the Technical Committee 95 of the IEEE International Committee on Electromagnetic Safety (www.ices-emfsafety.org). Since 2018, he has chaired the Board of Directors of the Mobile and Wireless Forum (www.mwfai.org), an international industry association supporting research into RF health and safety, and promoting wireless device accessibility.

GIORGI BIT-BABIK (Senior Member, IEEE) received the M.Sc. (Hons.) and Ph.D. degrees in radio physics and electronics from Tbilisi State University (TSU), Tbilisi, Georgia, in 1994 and 1998, respectively. He was a Research Staff Member and later an Associate Professor at TSU. In 2001, he joined the Electromagnetic Energy (EME) Research Laboratory, Motorola Inc., Fort Lauderdale, FL, USA. He is currently a Distinguished Member of the Technical Staff and a Motorola Innovators Circle (MIC) Member at Motorola Solutions, Inc. He holds 33 patents, mostly in antenna technology, and has published more than 90 journal and conference publications in applied electromagnetics and RF exposure dosimetry. His work is related to antenna technology research and development, RF exposure dosimetry, and compliance assessment and standards. He is a member of multiple working groups and project teams within ICES TC34 and TC106 and a Convenor of the JWG IEC/IEEE 62704-2. He serves as a Technical Advisor for USNC TAG106. He is actively involved in the IEEE ICES TC34 and TC95 and IEC TC106 standards committees, developing measurement and numerical methods for RF exposure assessment. He was a recipient of the IEC 1906 Award and the IEEE Standards Association International Award.

KEVIN SANDERSON received the Bachelor of Science degree in physics with minors in electrical engineering and computer science from the University of Illinois Urbana–Champaign, where he is currently pursuing the M.S.E.E. degree. As an Intern and a Co-Op at Motorola Solutions, Fort Lauderdale, FL, USA, he focused on RF dosimetry and computational electromagnetics, antenna design, and RF circuit optimization, contributing to several publications and one pending patent. He is particularly interested in research that connects physics with practical applications in computing and electrical systems.

PAOLA RUSSO (Senior Member, IEEE) received the Ph.D. degree in electronic engineering from the Polytechnic University of Bari, Bari, Italy, in April 1999. From January 2005 to July 2019, she was an Assistant Professor with the Polytechnic University of Marche (UnivPM), Ancona, Italy, where she was appointed as an Associate Professor, in August 2020. She teaches antenna design and fundamentals of electromagnetics. Her research interests include the application of numerical modeling to EMC problems, antenna problems, plasma antennas, and electromagnetic sensors. She is a member of Italian Society of Electromagnetics (SIEm) and the Scientific Board of Italian Center for the study of the interactions between electromagnetic fields and biosystems (ICEmB).

ALFREDO DE LEO (Senior Member, IEEE) was born in Bari, Italy, in 1975. He received the Graduate degree (summa cum laude) in electronic engineering and the Ph.D. degree in electromagnetism and bioengineering from the Università Politecnica delle Marche, Italy, in 1999 and 2014, respectively. He is currently with Università Politecnica delle Marche, where he teaches "industrial application of electromagnetic fields" and "electrical systems for renewable energy." His current research interests include the development of electromagnetic models, laboratory experiments, and numerical simulation techniques related to interactions between electromagnetic fields and biological beings, and remote sensing of physiological activities and reverberation chambers. He is a member of the IEEE Electromagnetic Compatibility Society, Italian Society of Electromagnetics (SIEm), and the Consorzio Nazionale Interuniversitario per le Telecomunicazioni (CNIT). He is an Expert Member of IET TC 77/JMT MU Technical Committee No. 77: Electromagnetic Compatibility, JMT MU: Measurement Uncertainty, and CEI Technical Subcommittees SC210/7713 and SC 210/A.

VALTER MARIANI PRIMIANI (Senior Member, IEEE) received the Laurea degree (summa cum laude) in electronic engineering from the University of Ancona, Ancona, Italy, in 1990.

He is currently a Full Professor in electromagnetic compatibility (EMC) with Università Politecnica delle Marche, Ancona, Italy. He is also a member of the Department of Information Engineering, where he is also responsible for the EMC Laboratory. He was involved in the European Project RISE-6G on the use of reconfigurable intelligent sustainable environments for 6G wireless networks. He is involved in the Doctoral Networks MSCA 2022 "NEPIT" as responsible for the Ancona Unit. His research interests include the prediction of digital printed circuit board radiation, the radiation from apertures, the electrostatic discharge coupling effects modeling, and the analysis of emission and immunity test methods. Since 2003, he has also been involved in research activities on the application of reverberation chambers for compliance testing, metrology applications, and multipath propagation emulation. He has been a member of the COST Action 1407 ACCREDIT on the characterization of stochastic emissions from digital equipment. He is Italian Member of the Joint Task Force CISPR/A/SC77B on Reverberation Chambers. He is a Senior Member of the IEEE EMC Society and a member of Italian Society of Electromagnetics. Since 2007, he has been an active member of some working groups for the development of IEEE Standards: 299.1, 1302, 2715, and 2716 on shielding effectiveness measurements. Since 2014, he has been a member of the International Steering Committee of EMC Europe. Since 2017, he has been the Chair of the working group for the IEEE Standard 2718 for the characterization of stochastic emissions. He is an Associate Editor of the journal *IET Science, Measurement and Technology*.

VALERIO DE SANTIS (Senior Member, IEEE) received the Laurea degree (summa cum laude) in telecommunication engineering and the Ph.D. degree in electrical and computer engineering from the University of L'Aquila, L'Aquila, Italy, in 2006 and 2010, respectively.

He joined the Foundation for Research on Information Technologies in Society, IT'IS Foundation, Switzerland, from 2011 to 2013, holding the position of Project Leader. He was an Assistant Professor at Nagoya Institute of Technology, Nagoya, Japan, from January 2015 to March 2015. He is currently an Associate Professor with the University of L'Aquila. He is participating in and leading several standardization efforts in the human exposure and product safety domain. His current research interests include wireless power transfer, numerical methods and techniques, electromagnetic compatibility (EMC), bioelectromagnetics, and human exposure safety, all testified by more than 100 papers published in peer-reviewed journals and conferences.

Prof. de Santis is a member of the BioElectroMagnetic (BioEM) Society, IEC TC 106. He was the Secretary of IEEE ICES TC95 SC6. He received the Second-Best Student Paper Award at the BioEM Annual Meeting, Cancun, Mexico, in 2006, the Best Student Paper Award at the IEEE International Symposium on EMC, Honolulu, USA, in 2007, the Best Poster Award at the IEEE Biennial Conference on Electromagnetic Field Computation (CEFC), Hangzhou, China, in 2018, and the 2025 Motohisa Kanda Award for the Most Cited Paper of IEEE TRANSACTIONS ON ELECTROMAGNETIC COMPATIBILITY in the past five years.